2016 SNMMI Highlights Lecture: Cardiovascular Nuclear Medicine

Nagara Tamaki, MD, PhD, Hokkaido University Graduate School of Medicine, Sapporo, Japan

From the Newsline Editor: The Highlights Lecture, presented at the closing session of each SNMMI Annual Meeting, was originated and presented for more than 30 years by Henry N. Wagner, Jr., MD. Beginning in 2010, the duties of summarizing selected significant presentations at the meeting were divided annually among 4 distinguished nuclear and molecular medicine subject matter experts. Each year Newsline publishes these lectures and selected images. The 2016 Highlights Lectures were delivered on June 15 at the SNMMI Annual Meeting in San Diego, CA. In this issue we feature the lecture by Nagara Tamaki, MD, PhD, from the Department of Nuclear Medicine at the Hokkaido University Graduate School of Medicine (Sapporo, Japan), who spoke on highlights in the cardiovascular sciences. Note that in the following presentation summary, numerals in brackets represent abstract numbers as published in The Journal of Nuclear Medicine *(2016;57[suppl 2]).*

The numbers of abstracts on cardiovascular topics presented at this year's SNMMI Annual Meeting were similar from North America (34), Asia (40), and Europe (46). Although the total number of cardiovascular presentations was slightly reduced in 2016 from 2015 (120 and 123, respectively), we saw a relative increase in abstracts from European countries (from 37 in 2015 to 46 in 2016). As in the previous year, we have seen a shift away from abstracts on myocardial perfusion imaging (MPI) toward molecular imaging, in both the basic sciences and in clinical practice. Such trends were nicely demonstrated in the Cardiovascular Young Investigator Award Symposium, at which 4 of 6 presentations were focused on atherosclerotic imaging using various molecular signals, with the remaining 2 presentations related to quantitative PET assessment. In addition, a special integrated session at the Annual meeting on translational molecular imaging in heart failure introduced multimodality imaging as well as multiple radiotracer imaging techniques for assessing the pathophysiology of myocardial dysfunction in heart failure. Marcelo Di Carli, MD, emphasized and summarized the importance of translational molecular imaging in heart failure at the end of that session.

Assessment of Atherosclerosis

Many investigators are involved in developing and researching possible targets and ligands in different aspects of arterial sclerosis, including but not limited to: thrombus, macrophages, T lymphocytes, smooth muscle cells, inflammatory cytokines, proliferative factors, oxidized low-density lipoprotein (LDL) and receptors, fibrinolytic proteases, serum proteins, cellular matrix, adhesion molecules, and apoptosis.

Nagara Tamaki, MD, PhD

Perez-Medina and colleagues from the Icahn School of Medicine at Mount Sinai (New York, NY), Memorial Sloan–Kettering Cancer Center (New York, NY), Academic Medical Center (Amsterdam, The Netherlands), and the University of Copenhagen (Denmark) reported on "Multimodal PET imaging of high-density lipoprotein (HDL) trafficking in multiple atherosclerosis models" [63]. HDL is involved in a plethora of biologic processes. Through extensive studies involving a unique set-up combining PET/CT and PET/MR imaging in murine, rabbit, and porcine atherosclerosis models, these researchers have demonstrated that ^{89}Zr labeling is a valuable tool for noninvasive assessment of pharmacokinetics and distribution of the main components of HDL (Fig. 1). They prepared reconstituted HDL discoidal nanoparticles and labeled them with ^{89}Zr by attaching it to either the apolipoprotein component, to yield ^{89}Zr-apoA-1-labeled HDL, or to a phospholipid chelator, to yield ^{89}Zr-phospholipid-labeled HDL (^{89}Zr-PL-HDL). They conducted extensive imaging, pharmacokinetic, and bidistribution studies in a double balloon injury/high-cholesterol rabbit model of atherosclerosis. PET/CT and PET/MR image analyses showed increased radioactivity concentration in the aortas of animals with atherosclerosis compared to controls. Ex vivo counting corroborated these findings, and increased radioactivity concentration was found in the aortas of animals with atherosclerosis for both nanoparticle agents. Finally, they tested ^{89}Zr-PL-HDL in a porcine model of atherosclerosis. Three animals were injected with ^{89}Zr-PL-HDL, and both PET/CT and PET/MR imaging were performed at 48 hours after injection. Whole-body PET imaging showed tracer accumulation in the inflamed femoral arteries, where lesions were induced by endothelial denudation. Autoradiography showed patchy radioactivity distribution and increased accumulation of radioactivity. The authors summarized their results by noting that "^{89}Zr labeling of HDL allows studying its in vivo behavior by noninvasive PET imaging, including visualization of its specific accumulation in the atherosclerotic vessel wall. This imaging tool, in combination with CT or MR imaging, allows noninvasive evaluation of HDL distribution and could be of great value in exploring its metabolism and trafficking in preclinical and clinical settings."

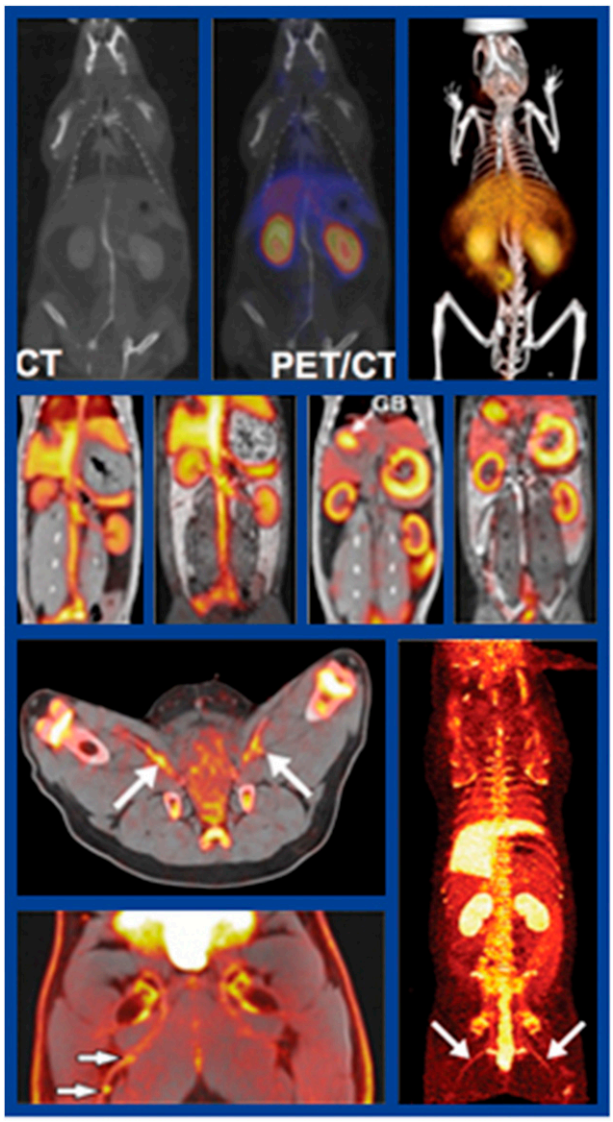

FIGURE 1. Multimodal PET imaging of high-density lipoprotein (HDL) trafficking in multiple atherosclerosis models. Top block: CT (left), ^{89}Zr-ZI-HDL PET/CT (middle), and fluorescent (right) imaging, as well as biodistribution and pharmacokinetic studies, were performed in apolipoprotein-E knockout mice and wild-type controls. Elevated radioactivity and fluorescence intensity were found in aortas of apoE knockout mice but not controls. Middle block: Similar studies, including ^{89}Zr-PL-HDL PET/CT and PET/MR imaging at 1 hour (left 2 images) and 48 hours (right 2 images), were conducted in a double-balloon–injury high-cholesterol rabbit model of atherosclerosis. Trends similar to those with the mouse data were noted, with ex vivo counting corroborating increased radioactivity concentrations in the aortas of both animal models for both nanoparticle agents. Bottom block: ^{89}Zr-PL-HDL imaging in a porcine model of atherosclerosis. Whole-body PET (right) at 48 hours showed tracer accumulation in the inflamed femoral arteries (arrows), where lesions were induced by endothelial denudation. PET/MR (left) indicated "hot spots" in the femoral arteries (arrows).

England and colleagues from the University of Wisconsin (Madison) and Seoul National University (Republic of Korea) reported on "Radiolabeled long-circulating nanoparticles for reassessing the enhanced permeability and retention effect in peripheral arterial disease" [65]. After surgical induction of hind limb ischemia in a murine model, the ischemic hind limb healed over a period of 15–20 days (Fig. 2). The authors assessed the passive targeting capabilities of ^{64}Cu-labeled PEGylated reduced graphene oxide–iron oxide nanoparticles (^{64}Cu-RGO-IONP-PEG) in PET imaging. PET imaging at 3, 10, and 17 days after surgery showed that RGO-IONP-PEG accumulated in the ischemic hind limb at higher levels soon after surgery, when the enhanced permeability and retention effect was highest. This accumulation diminished over time, with the lowest accumulation at day 17 postsurgery. Photoacoustic imaging confirmed the presence of nanoparticles within the ischemic hind limb after injection, whereas the nonischemic hind limb showed minimal accumulation (Fig. 3). These data further showed the potential utility of organic/inorganic hybrid nanoparticles for imaging of ischemia-related disease. The authors pointed toward potential use as a future theranostic agent, providing both imaging and therapeutic applications.

Derlin and colleagues from the Hannover Medical School (Germany) and the Technische Universität München (Garching, Germany) described their experience in "Imaging

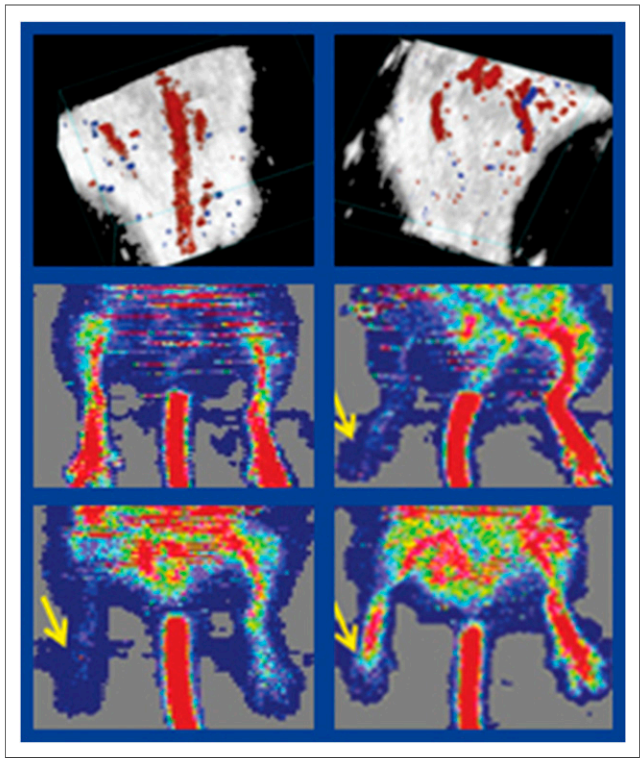

FIGURE 2. Murine model of peripheral arterial disease assessed using a hind limb ischemia model. Top: Doppler ultrasound imaging of nonischemic (left) and ischemic (right) hind limbs after surgical induction of ischemia. Bottom block of 4 images: Laser Doppler imaging showed vascularization of the hind limb (clockwise) before surgery, immediately postsurgery, at day 17 after surgery, and at day 3 after surgery. Vasculature normalized in 4–6 weeks after surgery.

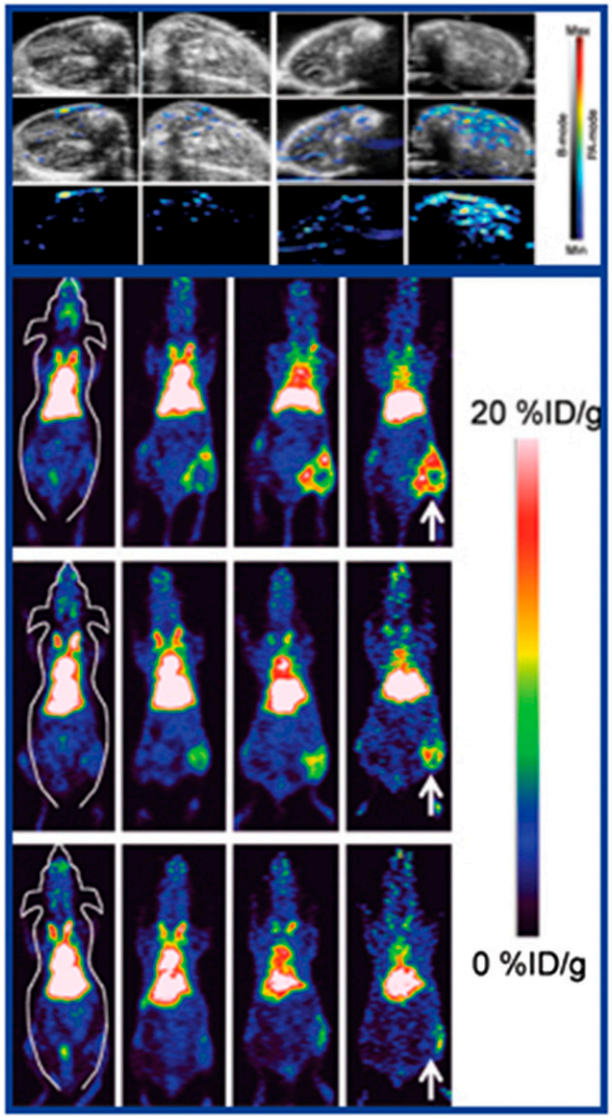

FIGURE 3. Multimodality imaging of RGO-IONP-PEG. Top block: Photoacoustic imaging, acquired before (left 2 columns) and 3 days after (right 2 columns) injection, confirmed the presence of nanoparticles within the ischemic hind limb (left in each column set), whereas the the nonischemic hind limb (right in each column set) showed minimal accumulation. Bottom block: Serial (3–72-h) PET imaging at days 3 (top row), 10 (middle row), and 17 (bottom row) showed that ^{64}Cu-RGO-IONP-PEG accumulated in the ischemic hind limb at higher levels directly after surgery, when the enhanced permeability and retention effect was highest. This accumulation diminished over time, with the lowest accumulation at day 17 postsurgery. These data further show the potential utility of organic–inorganic hybrid nanoparticles for imaging of ischemia-related diseases.

ruptured coronary atherosclerotic plaques by use of chemokine receptor type 4 (CXCR4)–targeted, motion-corrected PET/CT" [67]. ^{68}Ga-pentixafor, which specifically detects CXCR4(+) inflammatory cells, positively accumulated in culprit lesions (CT-identified locations of stents) but not in stable lesions (calcifications) in patients early after myocardial infarction (MI) (Fig. 4). In addition, dual-respiratory and electrocardiograph gating facilitated detection of culprit lesions when compared with single- or nongating acquisitions. Thus, targeted PET imaging with ^{68}Ga-pentixafor seems to be a promising noninvasive method for identification of ruptured and high-risk atherosclerotic plaques after MI.

Li and colleagues from the Medical University of Vienna (Austria) and the Vienna General Hospital (Austria) reported on "Combined ^{18}F-FDG PET/CT and ^{18}F-NaF PET/CT imaging in assessing vascular inflammation and osteogenesis in calcified atherosclerotic lesions" [68]. The study included 34 oncology patients who underwent imaging with both agents, with subsequent analysis of 8 segments of large cardiac arteries and classification of lesions as noncalcified, mildly calcified, and severely calcified at different stages of atherosclerosis. Increased target-to-background ratios (TBRs) for FDG were found in noncalcified lesions in the early stages of atherosclerosis, whereas corresponding enhanced NaF TBRs were found in early noncalcified lesions and also in advanced, severely calcified lesions. Higher linear regression ratios ($r = 0.6$) were found in mildly calcified lesions. Figure 5 shows representative images of different lesions with distinctive behaviors of both tracers during the progression of atherosclerosis from baseline to follow-up imaging. In most relatively early atherosclerotic lesions (noncalcified and mildly calcified lesions), inflammation and osteogenesis developed in parallel. In severely calcified lesions, however, inflammation and osteogenesis developed discordantly. They concluded that inflammation estimated by ^{18}F-FDG uptake and osteogenesis assessed by NaF uptake might predict atherosclerosis-prone segments. Inflammation and osteogenesis may develop in parallel in the propagation phase, but high calcium density with limited inflammation is seen in end-stage disease. Thus, increased osteogenesis with reduced inflammation might predict stabilizing or retarding of plaque.

Many of us are quite excited to see the potential for identifying and exploring aspects of active atherosclerosis using new radiotracers, with much of this research being carried out in animal studies. At the same time, we must select suitable agents that address a range of pertinent clinical questions, such as identifying highly vulnerable or high-risk plaque, assessing treatment monitoring, selecting optimal treatment strategies, etc. In addition, FDG and NaF are most commonly used for identifying atherosclerotic lesions in the clinical setting. FDG may identify active inflammation, whereas NaF may identify osteogenesis. It would be nice to see significant differences in tracer uptake under a range of conditions and settings. Moreover, precise comparison may be needed with other modalities, such as MR imaging, optical imaging, and ultrasound to define optimal selection of imaging techniques for various clinical settings.

Assessment of Myocardial Dysfunction

A number of studies presented at SNMMI 2016 demonstrated myocardial dysfunction using various molecular probes. Taki and colleagues from Kanazawa University

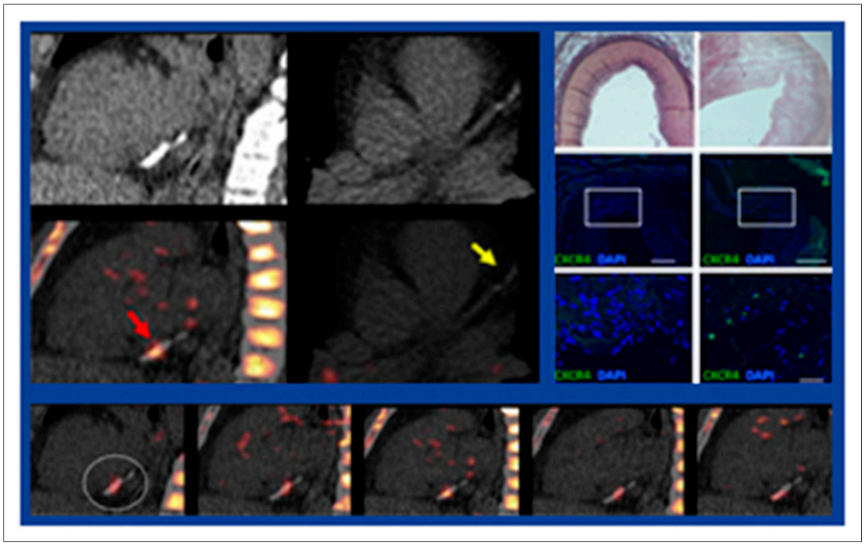

FIGURE 4. CXCR4-targeted imaging of ruptured coronary plaques. ^{68}Ga-pentixafor specifically detects CXCR4(+) inflammatory cells accumulated in culprit lesions (red arrows) but not stable lesions (yellow arrow) in patients early after myocardial infarction. Top left block: ^{68}Ga-pentixafor PET/CT 5 days after reperfusion stent. Top right block: Validation in human cadaver coronaries. Left, control; right, plaque. Bottom block: Motion correction technique (gating), left to right: none, electrocardiograph, dual, respiratory (amp), and respiratory (data), with corresponding plaque detection rates of 32%, 68%, 85%, 81%, and 54%. Target PET imaging with ^{68}Ga-pentixafor is a promising method for identification of ruptured coronary plaque.

(Japan), Mie University (Tsu, Japan), the Cardiology National Center for Global Health and Medicine (Tokyo, Japan), and Saitama Medical University Hospital (Irumagun, Japan) described "Revisiting RGD uptake after MI: does it reflect inflammatory change or angiogenesis or both?" [397]. The researchers serially assessed tracer uptake after MI in rats to determine whether ^{125}I-RGD imaging reflected inflammatory or angiogenesis changes or both. ^{125}I-RGD uptake in the identified area at risk was weak at day 3 after MI, peaked at day 7, and persisted at day 14 and at 1 month (Fig. 6). Histopathologic analysis showed macrophage infiltration by CD68 peaking at day 3, followed by rapid reduction from day 14 to 1 month. Myofibroblast appearance and microvessel formation were minimal at day 3 but markedly increased at day 7, followed by gradual reduction until 1 month, which correlated well with RGD uptake. Therefore, ^{125}I-RGD uptake corresponded to myofibroblast appearance and vessel-like formation throughout the post-MI process. This research suggests that iodinated RGD uptake may reflect angiogenesis and not merely inflammation after the acute phase of MI, with the potential for monitoring various treatment strategies in this setting.

A number of reports at the meeting addressed the use of ^{18}F-FDG PET in cardiac sarcoidosis and other active myocardial disorders. A well-attended continuing education session on "Detection and assessment of cardiac sarcoidosis by FDG PET" was sponsored by the Japanese Society of Nuclear Medicine. Presenters discussed optimization of patient preparation to inhibit physiologic myocardial uptake, quantitative assessment of cardiac uptake, and patient monitoring by ^{18}F-FDG PET as well as delayed enhancement of MR imaging. Japanese guidelines for cardiac sarcoidosis were also introduced and discussed. Dr. Di Carli concluded the session by reviewing U.S. perspectives on management of cardiac sarcoidosis. Many nuclear physicians are challenged by the process of inhibiting physiologic ^{18}F-FDG uptake sufficiently to differentiate it from abnormal uptake in active sarcoid lesions. Japanese guideline suggest >15-hour (preferably >18-hour) fasting with a low-carbohydrate diet, whereas many U.S. investigators prefer a high-fat diet to fasting in order to minimize physiologic myocardial uptake of ^{18}F-FDG.

Manabe and colleagues from Hokkaido University (Sapporo, Japan) and the National Institute of Radiological Sciences (Chiba, Japan) reported that "Steroid therapy affects the cardiac metabolic shift and requires careful attention in evaluation of cardiac sarcoidosis with FDG PET/CT" [13]. The study included 21 patients with cardiac sarcoidosis, and a representative case indicated focal uptake in the left ventricle with multiple other areas of ^{18}F-FDG uptake in the supraclavicular, hilar, mediastinum, and abdominal lymph nodes and lungs before treatment. Images were acquired with low-carbohydrate diets after 18-hour fasting. Imaging was repeated after treatment. After steroid therapy, extracardiac uptakes were reduced but relative diffuse cardiac uptake was seen, which was believed to be physiologic and therefore a false-positive finding (Fig. 7). Blood sampling data indicated that the fasting plasma glucose level at the second scan was slightly higher but did not reach statistical significance. However, free fatty acid was significantly lower and the immune-reactive insulin level was significantly higher at the second scan. These data indicate that after steroid treatment, long fasting with a low-carbohydrate diet preparation may not perfectly suppress physiologic FDG uptake in the myocardium because of the metabolic shift from fatty acid to glucose. A number of studies address the clinical value of ^{18}F-FDG PET for detecting cardiac sarcoidosis and for assessing treatment monitoring. Abnormal cardiac FDG uptake resulting from active inflammation should be carefully differentiated from physiologic FDG uptake in the myocardium. Blood sampling data may help in such differentiation.

Sympathetic neurotransmission imaging has been used in patients with heart failure and various myocardial disorders

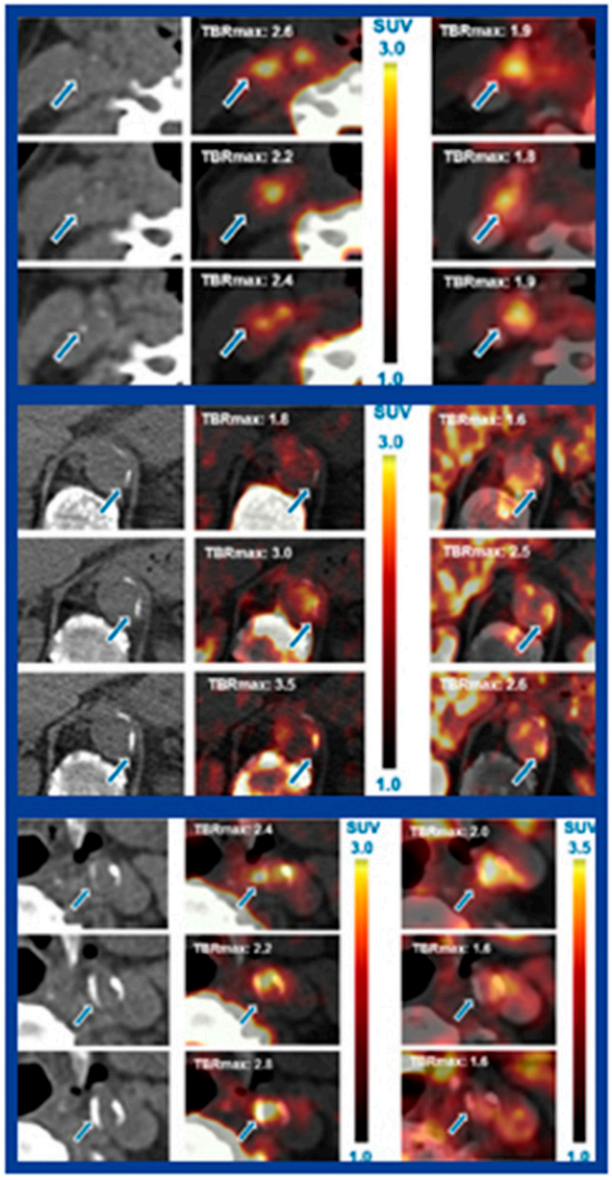

FIGURE 5. Combined ^{18}F-FDG PET/CT and ^{18}F-NaF PET/CT imaging in vascular inflammation and osteogenesis in calcified atherosclerotic lesions. Representative images of noncalcified (top block), mildly calcified (middle block), and severely calcified (bottom block) lesions during progression of atherosclerosis from baseline (top row in each block) to 12 months (middle rows), to 24 months (bottom rows). Imaging acquired with (left to right in each block) CT, ^{18}F-NaF PET/CT, and ^{18}F-FDG PET/CT. In relatively early atherosclerotic lesions (noncalcified and mildly calcified lesions), inflammation and osteogenesis generally developed in parallel. In severely calcified lesions, inflammation and osteogenesis developed discordantly, as seen with the relative tracer uptake values.

in order to identify high risk for sudden cardiac death or fatal arrhythmias and to optimize treatment strategies in the clinical setting. ^{11}C-hydroxyephedrine (^{11}C-HED) and ^{123}I-metaiodobenzylguanidine (^{123}I-MIBG) are used for assessing presynaptic function, and^{11}C-CGP 12177 is used to assess β-receptor function. Aikawa and colleagues from Hokkaido University Graduate School of Medicine (Sapporo, Japan) reported that "Impairment of myocardial sympathetic innervation and its heterogeneity are associated with diastolic dysfunction in patients with heart failure and preserved ejection fraction: ^{11}C-HED PET study" [231]. Typical examples of ^{11}C-HED uptake with quantitative parameters and retention index are included in Figure 8. Although the ^{11}C-HED retention index is relatively preserved in heart failure patients with mild diastolic dysfunction, its retention was severely reduced, with heterogeneous distribution in the myocardium, in patients with moderate diastolic dysfunction. Logistic regression analyses indicated that both impaired sympathetic innervation and its heterogeneity were novel predictors of diastolic dysfunction in heart failure patients with preserved systolic function, which highlights the role of sympathetic activation in heart failure in these patients.

Nakajima and colleagues from Kanazawa University (Japan), Diagram Consulting (Kihei, HI), and Hakodate-Goryoukaku Hospital (Japan) presented a "Cardiac mortality risk chart in chronic heart failure: multivariate ^{123}I-MIBG risk model incorporating correction of collimator distances" [227]. These researchers standardized the ^{123}I-MIBG uptake as a heart-to-mediastinum ratio (H/M) for different collimators using calibration based on 225 data acquisition conditions in phantoms. Data from 1,322 patients with chronic heart failure at multiple centers in Japan over a mean follow-up of 6.5 years were analyzed to provide multivariate 2- and 5-year mortality risk models, depending on MIBG H/M, New York Heart Association class, left ventricular ejection fraction, and age. Their table showed the resulting 5-year cardiac mortality rate based on various ^{123}I-MIBG and clinical parameters. This is an important study, and it would be interesting to see the results of similar data analyses in a patient population from Europe or the United States.

Methodologic Challenges

A number of reports highlighted new applications of cardiac-dedicated gamma cameras for cardiovascular nuclear medicine. Miyagawa and colleagues from Ehime University School of Medicine (Japan) reported on "^{123}I-MIBG H/Ms obtained by DNM530c cadmium-zinc-telluride (CZT) SPECT: direct comparison with conventional planar imaging" [229]. In 84 consecutive patients with suspected Parkinson disease, early (10-minute) and delayed (5-hour) conventional planar acquisitions were followed by cardiac SPECT. A series of coronary slices were summed to calculate the H/Ms. Good correlation was seen between conventional and cardiac camera H/Ms in both early and late imaging. In addition, the ^{123}I-MIBG washout was also well correlated. The authors concluded that semiquantitative analysis of ^{123}I-MIBG uptake and kinetics may be feasible with the dedicated cardiac SPECT camera (Fig. 9).

The most exciting application of dedicated cardiac SPECT was reported by Thackeray and colleagues from Hannover

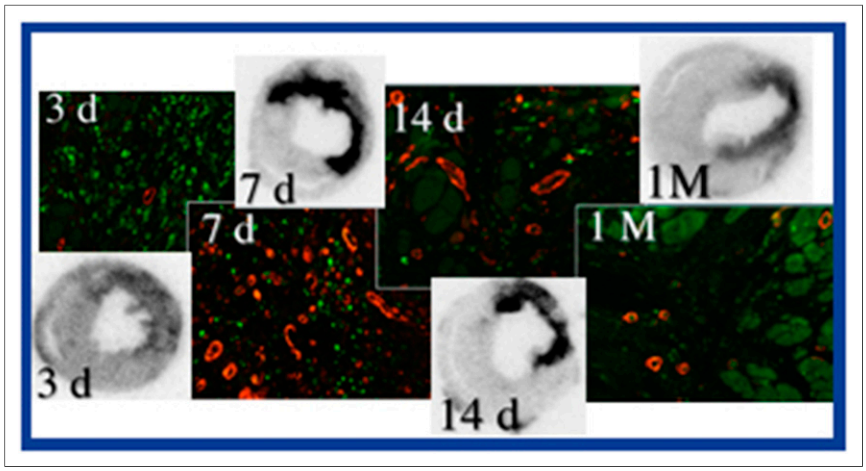

FIGURE 6. RGD, inflammation, and angiogenesis. ^{123}I-RGD imaging and histopathologic analysis at (left to right) days 3, 7, and 14 and 1 month after myocardial infarction (MI). Macrophage infiltration by CD68 (green) peaked at day 3, followed by rapid reduction up to 1 month. Anti–smooth muscle α-actin (myofibroblasts, green) and microvessel formation were minimal at day 3 but markedly increased at day 7, followed by gradual reduction up to 1 month, which correlated well with RGD uptake throughout the post-MI process.

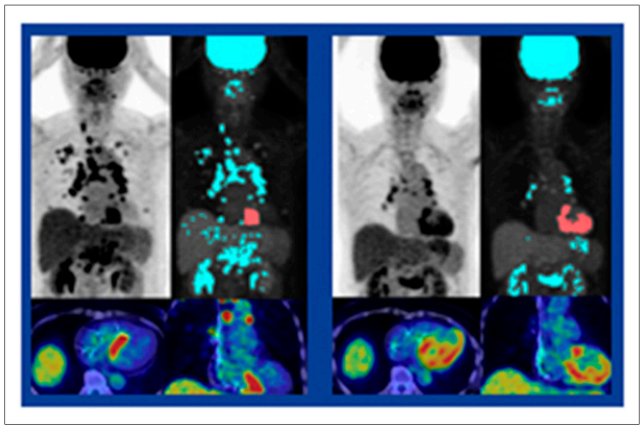

FIGURE 7. Steroid therapy and ^{18}F-FDG PET/CT evaluation of cardiac sarcoidosis. Representative imaging before (left block) and after (right block) steroid treatment in a patient with cardiac sarcoidosis. Before treatment, multiple areas of focal uptake were visible in the left ventricle and in the supraclavicular, hilar, mediastinal, and abdominal lymph nodes and lungs. After 1 month of steroid therapy, extracardiac uptakes were reduced, and relatively diffuse cardiac uptake was believed to be physiologic (i.e., false-positive).

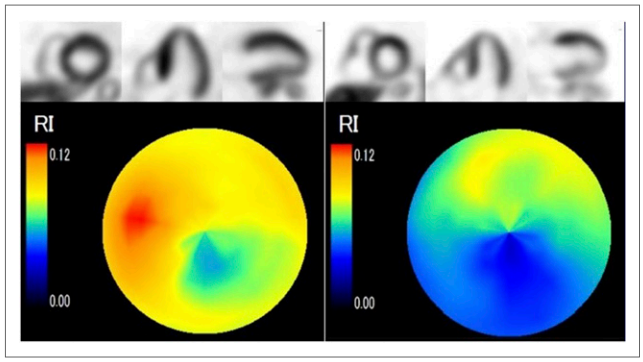

FIGURE 8. ^{11}C-hydroxyephedrine (^{11}C-HED) PET and myocardial sympathetic innervation in diastolic dysfunction in heart failure. Typical examples of ^{11}C-HED uptake with quantitative parameters and retention indices are shown for mild dysfunction (left block) and moderate dysfunction (right block). Although the retention index was relatively preserved in mild diastolic dysfunction, tracer retention was severely reduced with heterogeneous distribution in the myocardium in moderate dysfunction.

University Medical School (Germany), who described the "Suitability of ^{99m}Tc-teboroxime CZT SPECT for quantitative MPI—comparison with ^{99m}Tc sestamibi in mice" [121]. Healthy and postinfarct mice were scanned on consecutive days with inhouse-synthesized ^{99m}Tc-teboroxime and commercially purchased ^{99m}Tc-sestamibi. Serial pinhole collimator scans with short acquisition (2 seconds/view) per collimator position were analysed as a dynamic sequence (during a total of 20 minutes acquisition time). Rapid uptake and washout of ^{99m}Tc-teboroxime showed higher early contrast to liver and favorable kinetics for quantification of myocardial blood flow. Sestamibi uptake was sustained with lower initial contrast to liver. More rapid uptake and washout of teboroxime is consistent with its high extraction fraction and clearance (Fig. 10). Thus, dynamic perfusion imaging is feasible with the CZT SPECT system. I believe that quantitative measurement of myocardial blood flow and flow reserve is available with accuracy similar to that of PET when high-speed CZT SPECT imaging is combined with a high-extraction-fraction ^{99m}Tc perfusion agent.

Ko and colleagues from National Taiwan University Hospital (Taipei City and Yunlin County) and the Far Eastern Memorial Hospital (New Taipei City, Taiwan) reported on "The gender-specific effects of patient positioning on the diagnostic performance of MPI using a CZT SPECT camera" [285]. The path of detected photons may be altered by changes in patient positioning in a CZT camera, and some perfusion defects may be attributed to positioning, with resulting effects on diagnostic performance, specifically with multipinhole CZT scanners. These researchers showed color spots representing areas under the curve for diagnostic performance based on location, sex, and body mass index (BMI) (Fig. 11). They demonstrated clear differences in diagnostic accuracy of MPI using this CZT camera, depending on the location and severity of perfusion defects, sex, and BMI, most likely

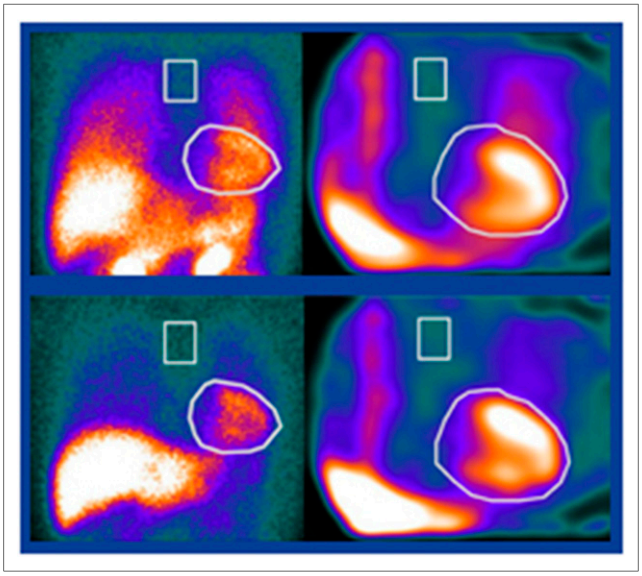

FIGURE 9. ^{123}I-MIBG heart-to-mediastinum ratios (H/Ms) obtained with cadmium-zinc-telluride (CZT) SPECT. Top: early (10-minute) planar (left) and early (10-minute) (right) SPECT. Bottom: delayed (5-hour) (left) planar and (right) SPECT. A series of coronary slices were summed to calculate H/Ms. Good correlation was seen between conventional planar and CZT images in both early and late imaging.

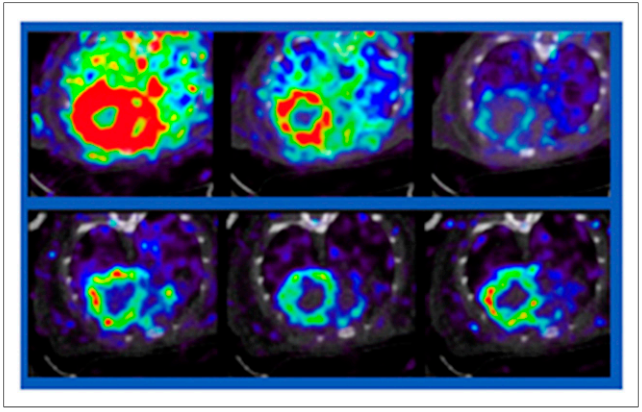

FIGURE 10. Pinhole CZT SPECT rapid dynamic imaging of healthy and infarcted mice after injection of inhouse-synthesized ^{99m}Tc-teboroxime (top) and commercially purchased ^{99m}Tc-sestamibi (bottom) at (left to right) 180, 270, and 450 seconds after injection. Rapid uptake and washout of ^{99m}Tc-teboroxime showed higher early contrast to liver and favorable kinetics for quantitation of myocardial blood flow. ^{99m}Tc-sestamibi uptake was sustained, with lower initial contrast to liver. Rapid uptake and washout of ^{99m}Tc-teboroxime was consistent with the tracer's high extraction fraction and clearance.

as a result of strikingly different sensitivities in surface and deep areas and also in central and peripheral fields. It may be useful to consider whether CZT scanner imaging in the prone position might solve such diagnostic differences.

Conclusions

I believe that 4 major elements are driving nuclear medicine forward today: instrument development, data analysis improvement, drug development, and new clinical applications (Fig. 12). These elements constitute 4 "wheels" that provide balanced and safe movement forward—whether the metaphorical car is American, German, or Japanese. The situation is similar in nuclear cardiology. In the 2016 nuclear cardiology session, we saw cardiac-dedicated CZT cameras and SPECT blood flow measurement as examples of instrumentation and data analysis development. Molecular imaging with a variety of new agents is now assessing vulnerable plaque and various myocardial disorders. In addition, new clinical applications are being used or are in development for vulnerable plaque, heart failure, cardiac sarcoidosis, and amyloidosis. With continued development and integration of these 4 elements, the benefits of nuclear cardiology are likely to grow and expand in the future.

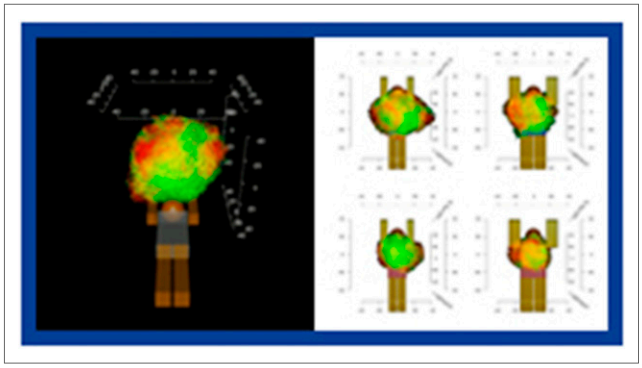

FIGURE 11. Sex-specific effects of patient positioning on myocardial perfusion imaging with a cadmium-zinc-telluride SPECT camera. Color spots represent areas under the curve (AUCs) for diagnostic performance based on location, sex, and body mass index (BMI) (AUCs: green = 0.8–1.0; yellow = 0.7–0.8; orange = 0.6–0.7; red = 0.5–0.6). Left: all patients. Right block: top, men; bottom, women; left, BMI $<$ 27; right, BMI $\geq$ 27. Some perfusion defects may be attributed to positioning, which may affect diagnostic performance in multipinhole CZT scanners.

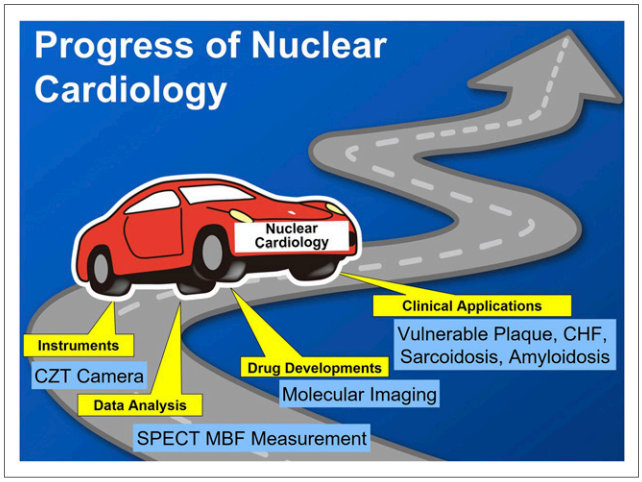

FIGURE 12. Progress of nuclear cardiology. Four major elements drive nuclear medicine and nuclear cardiology forward.